Geoscience Frontiers 11 (2020) 2003–2015

HOSTED BY

Contents lists available at ScienceDirect

Geoscience Frontiers

journal homepage: www.elsevier.com/locate/gsf

Research Paper

Apatite U–Pb dating and geochemistry of the Kyrgyz South Tian Shan (Central Asia): Establishing an apatite fingerprint for provenance studies

Stijn Glorie [a,*], Samantha March [a], Angus Nixon [a], Fun Meeuws [a], Gary J. O'Sullivan [b], David M. Chew [c], Christopher L. Kirkland [d], Dmitry Konopelko [e,f], Johan De Grave [g]

[a] Department of Earth Sciences, School of Physical Sciences, The University of Adelaide, SA, 5005, Australia
[b] UCD School of Earth Sciences, University College Dublin, Dublin, Ireland
[c] Department of Geology, Trinity College Dublin, College Green, Dublin, Ireland
[d] School of Earth and Planetary Sciences, Curtin University, Perth, 6845, Australia
[e] Saint Petersburg State University, 7/9 University Embankment, SPb-199034, Russia
[f] Novosibirsk State University, 1 Pirogova St., Novosibirsk, 630090, Russia
[g] Laboratory for Mineralogy and Petrology, Department of Geology, Ghent University, 281-S8 Krijgslaan, Ghent, 9000, Belgium

ARTICLE INFO

Handling Editor: M. Santosh

Keywords:
Apatite provenance
Central Asian Orogenic Belt
Tian Shan
Tarim Basin
Ferghana Basin

ABSTRACT

This paper presents an apatite U–Pb and geochemistry archive for exposed plutons and metamorphic rocks of the Kyrgyz South Tian Shan (STS) within the Central Asian Orogenic Belt. Apatite U–Pb dates and trace-element geochemistry are provided for 17 samples from late Carboniferous–early Permian I-type granites in the Terktinsky complex and A-type granites in the Kokshaal Range; early Devonian granites in the Kembel complex; Cryogenian granitoids and tuffs from the Middle Tian Shan and gneisses from the Atbashi metamorphic complex. These samples form a comprehensive selection of igneous and metamorphic rocks within the cores of Mesozoic basement highs that supplied detritus to adjacent basins such as the Tarim, Ferghana and Yarkand-Ferghana Basins. Generally, the granitoid samples preserve primary igneous apatite U–Pb ages that are within uncertainty of previously published zircon U–Pb dates. The apatites from the Atbashi metamorphic complex record anomalous Ordovician dates with large uncertainties that are interpreted as mixing ages between Cryogenian protolith formation and Carboniferous metamorphism. Principal component analysis discriminates apatite samples from the different bedrock terranes in the Kyrgyz STS based on their geochemical fingerprint and categorizes the samples with respect to an extensive apatite geochemical archive. The combined apatite-zircon archive provides a novel framework for provenance studies on the Meso–Cenozoic sedimentary history of the Central Asian Orogenic Belt.

1. Introduction

Sediment provenance studies commonly utilize detrital zircon grains, which preserve a geochronological and geochemical fingerprint of the tectonic history of the eroding hinterland (e.g. Lease et al., 2007; Condie et al., 2009; Gehrels, 2011; Cawood et al., 2012; Glorie et al., 2014). Given their extreme robustness to weathering, zircons are well suited for provenance studies, however, they have limitations. Zircons tend to crystallize from relatively evolved, silica-rich magmas (e.g. Belousova et al., 2002b), introducing a bias in the provenance record with respect to the SiO_2 concentration of the source rock. Differential zircon fertility (e.g. the presence of exceptionally zircon-rich rocks) may further enhance such bias (e.g. Moecher and Samson, 2006). Apatite crystals are commonly observed in clastic rocks and are increasingly used in provenance studies as they record complementary information to zircon grains concerning the tectonic history of the hinterland (e.g. Mark et al., 2016; Gillespie et al., 2018; O'Sullivan et al., 2018), for the following reasons: (1) Apatites are not as physically robust as zircons and are therefore more likely to represent less reworked detritus (e.g. Chew et al., 2011). (2) The U–Pb system in apatite resets at ~550–350 °C (Chew et al., 2014; Chew and Spikings, 2015) and, therefore, different tectonic events such as thermal overprints associated with regional metamorphism can be detected (Kirkland et al., 2017; Henrichs et al., 2018). (3) The trace element composition of apatite allows the nature of the source rock

* Corresponding author.
E-mail address: stijn.glorie@adelaide.edu.au (S. Glorie).
Peer-review under responsibility of China University of Geosciences (Beijing).

https://doi.org/10.1016/j.gsf.2020.06.003
Received 19 January 2020; Received in revised form 21 May 2020; Accepted 10 June 2020
Available online 16 July 2020

(protolith type, SiO_2 content, and the extent of metamorphic or metasomatic overprints) to be evaluated (e.g. Belousova et al., 2002; Jennings et al., 2011; Gillespie et al., 2018; Henrichs et al., 2018; O'Sullivan et al., 2018; Glorie et al., 2019). (5) Apatites can be double or even triple dated (U–Pb, fission track, U-Th-Sm/He), allowing a reconstruction of the thermal history of the rock from ~550 °C to near-surface temperatures (e.g. Carrapa et al., 2009; Glorie et al., 2017a,b; Jepson et al., 2018). Hence, combined apatite thermochronology and trace element geochemistry can provide complementary information about source terranes that cannot be accessed with information derived solely from zircons. However, before such provenance studies can be conducted, the apatite crystals in the basement source terranes need to be dated and geochemically characterised.

This study focusses on the Kyrgyz South Tian Shan (STS), the roof of the world's largest and most active intracontinental orogen (Abdrakhmatov et al., 1996), which was a major source terrane for the Mesozoic sediments in the adjacent Tarim, Ferghana and Yarkand-Ferghana Basins (De Pelsmaeker et al., 2018; Morin et al., 2018; Fig. 1). The timing of basement crystallization and exhumation of the Kyrgyz STS have extensively been studied by the means of zircon U–Pb geochronology

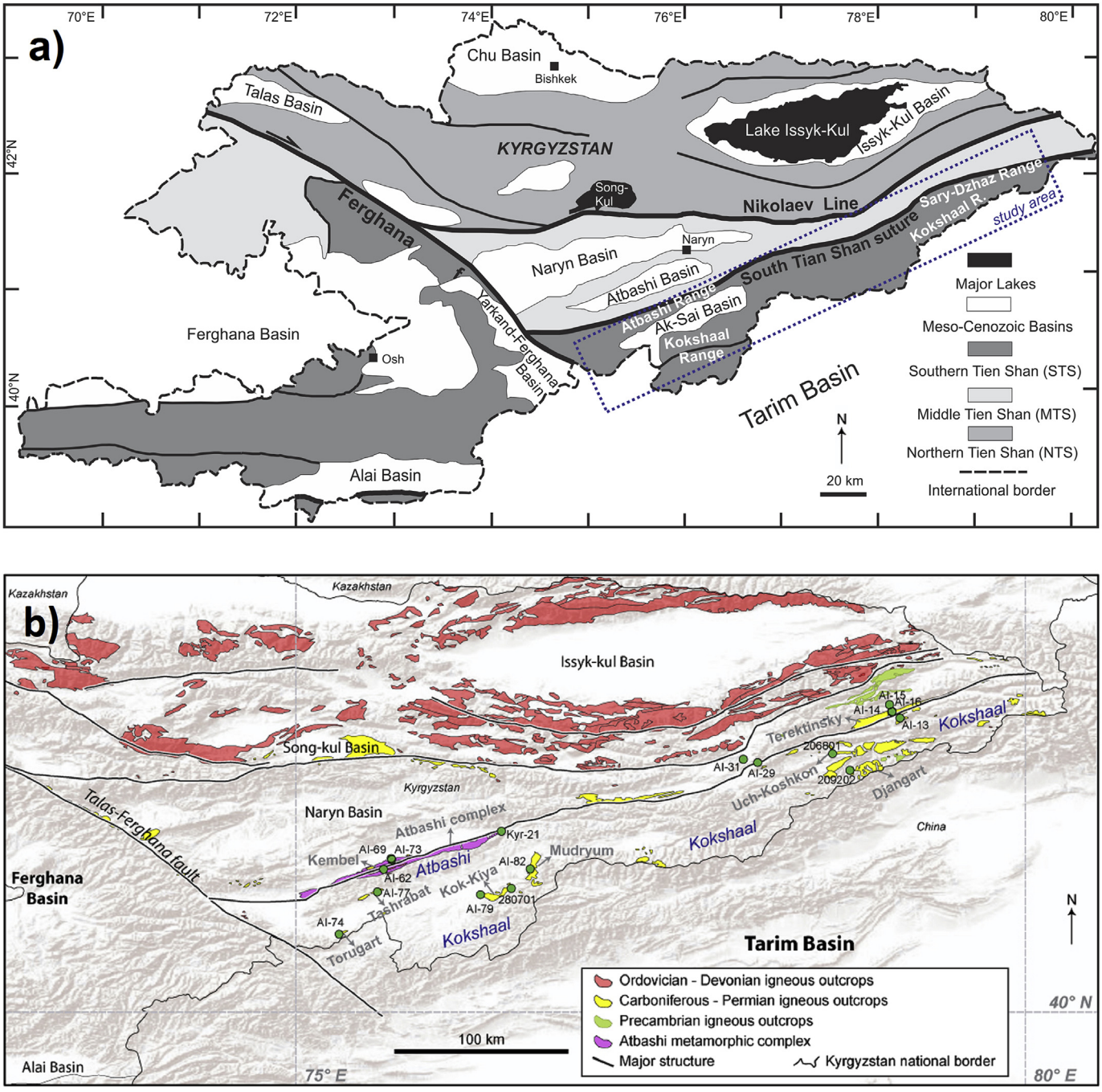

Fig. 1. (a) Simplified tectonic map of Kyrgyzstan showing the main basement terrane subdivisions and the major Meso–Cenozoic basins. The sampled mountain ranges for this study are indicated on the map in white font (the Sary-Dzhaz Range and Atbashi Range along the South Tian Shan suture and the Kokshaal Range in the South Tian Shan) (modified from De Grave et al., 2013). (b) Digital elevation model of the Kyrgyz Tian Shan overlain by the main igneous and metamorphic complexes, colour-coded by age (from Zhukov et al., 2008). The sampled complexes are named in grey font. Sample location for this study, within the Kyrgyz South Tian Shan (STS), are indicated by green symbols.

(Konopelko et al., 2007, 2009, 2017, 2018; Seltmann et al., 2011) and apatite fission track (AFT) and zircon/apatite U-Th-Sm/He (ZHe/AHe) thermochronology (Sobel et al., 2006; Glorie et al., 2011; De Grave et al., 2012; Macaulay et al., 2014; Jia et al., 2015; Nachtergaele et al., 2018). These datasets have revealed important aspects of both the high temperature (crystallization/metamorphism) and low-temperature thermal history of the Kyrgyz STS. However, tectonic processes that act in the temperature window between ~800 °C and ~200 °C have thus far only received little attention through limited mica Ar–Ar studies (e.g. Simonov et al., 2008; Hegner et al., 2010).

In this work, we present apatite U–Pb dates coupled with trace element geochemistry for 17 igneous and metamorphic samples from the Kyrgyz STS that have been previously dated by zircon U–Pb geochronology (Konopelko et al., 2007; Glorie et al., 2011). Furthermore, we use principal component analysis on this combined dataset to fingerprint the temporal and geochemical nature of the apatites in the STS basement (O'Sullivan et al., 2018). The new apatite archive improves our understanding of the mid-crustal thermal history of the Kyrgyz STS and provides a framework for future sedimentary provenance studies that incorporate information from detrital apatites.

2. Geological setting

The geological setting of the Kyrgyz South Tian Shan is extensively described in Konopelko et al. (2007, 2009), Glorie et al. (2011) and Seltmann et al. (2011) and the reader is referred to these papers for a detailed overview. Here, the description is limited to the regional context and the tectonic units that are relevant to the paper.

The Kyrgyz Tian Shan can be subdivided into three main tectonic units: the North Tian Shan (NTS), Middle Tian Shan (MTS) and South Tian Shan (STS) (Fig. 1). The NTS represents the southern extent of the Precambrian Palaeo-Kazakhstan continent (Windley et al., 2007) that was intruded by numerous Cambrian–Silurian (Caledonian) granitoids during closure of the Terskey Ocean at that time (Seltmann et al., 2011; De Grave et al., 2013). The MTS represents a Precambrian micro-continent that accreted to the NTS during closure of the Terskey Ocean (Seltmann et al., 2011). South of the MTS, the STS represents a Late Paleozoic accretionary complex between the Tarim and Palaeo-Kazakhstan microcontinents, which developed during the Carboniferous–Permian (Hercynian) in response to the closure of the Turkestan Ocean and the termination of the ancestral Tian Shan orogeny (Konopelko et al., 2007; Seltmann et al., 2011). The South Tian Shan suture forms the ophiolite-bearing relic of the Turkestan Ocean between the MTS and STS (Fig. 1; Glorie et al., 2011 and references therein). During the Meso–Cenozoic, the Kyrgyz Tian Shan was affected by several phases of punctuated intracontinental deformation related to tectonic events at the distant southern Eurasian margin (e.g. Sobel et al., 2006; Glorie et al., 2010, 2011; De Grave et al., 2012, 2013; Macaulay et al., 2014; Glorie and De Grave, 2016; Nachtergaele et al., 2018).

Samples for this study were targeted from igneous and metamorphic basement outcrops that compose the three main mountain ranges along the STS suture (the Sary-Dzhaz and Atbashi Ranges) and within the Kyrgyz section of the STS (the Kokshaal Range). Following the thermochronological literature, cited above, as well as the palaeotopographic reconstructions in De Pelsmaeker et al. (2018) and Morin et al. (2018), these areas were basement highs during the Jurassic–early Cretaceous and supplied detritus to adjacent basins such as the Ferghana, Yarkand-Ferghana and northern Tarim Basins at that time (Fig. 2). The Sary-Dzhaz Range (Figs. 1 and 2) developed along the eastern extent of the Kyrgyz STS suture and is largely composed of Cryogenian (~850–800 Ma) mylonitic-granitic rocks in the MTS and late Carboniferous–early Permian (~307–294 Ma) granites of the Terektinsky complex in the STS (Fig. 2; Konopelko et al., 2009; Glorie et al., 2011). The Kokshaal Range (Figs. 1 and 2) spans the southern margin of the Kyrgyz STS, to the east of the Talas-Ferghana fault, and hosts a number of early Permian (~299–279 Ma; mostly A-type) intrusions such as the Tashkoro, Uch-Koshkon, Djangart, Mudryum, Torugart and Kok-Kiya granitoids (Fig. 2; Konopelko et al., 2007; Glorie et al., 2011). The Atbashi Range (Figs. 1 and 2) developed along the STS suture and is composed of Carboniferous ophiolitic and metamorphic rocks (including ~328–319 Ma eclogite/blueschist) of the Atbashi Complex (Simonov et al., 2008; Loury et al., 2018) and the early Devonian (~417–410 Ma) granitic Kembel massif (Glorie et al., 2011). In addition, the smaller Permian Tashrabat intrusion (~286 Ma) forms part of the southern slopes of the Atbashi Range (Fig. 2; Glorie et al., 2011). All these basement highs were progressively exhumed to the surface during Meso–Cenozoic (~200–10 Ma) deformation as attested by apatite fission track thermochronology constraints (Sobel et al., 2006; Glorie et al., 2011; Macaulay et al., 2014; Jia et al., 2015; Glorie and De Grave, 2016), and can thus be regarded as suppliers of detritus to the Meso–Cenozoic deposits of adjacent basins, such as the Early Jurassic Yarkand-Ferghana Basin to the west (recording >3 km of Jurassic sediments) and the Tarim Basin to the south (recording >5 km Meso–Cenozoic sediments) (Watson et al., 1987; Otto, 1997; Sobel, 1999; Zhu et al., 2005; Ding, 2006; Yang et al., 2014; Jia et al., 2015; De Pelsmaeker et al., 2018; Morin et al., 2018; Nachtergaele et al., 2018). More recently, Morin et al. (2020) suggested that the main source terrane for the sediments in the Yarkand-Ferghana Basin was to the west during the Jurassic, however the relation between the steep relief to the East of the Talas-Ferghana fault (Fig. 2) and the apparent lack of sediment supply to the Yarkand-Ferghana Basin remains to be explained. Given the great similarity in zircon U–Pb ages for STS source rocks, the zircon U–Pb dataset cannot provide unique provenance constraints. To overcome this limitation, this paper characterizes the basement rocks for their apatite U–Pb geochronology and geochemistry, thus providing an improved framework for future provenance studies.

3. Methodology

Apatite crystals were sourced from existing mounts that were previously analysed for fission track thermochronology (Glorie et al., 2011a) or from separates that were used for zircon U–Pb dating (Konopelko et al., 2007). Trace element concentrations and U–Pb isotopes were measured on a RESOlution-LR 193 nm excimer laser coupled to an Agilent 7900 ICPMS system, following the analytical procedures and instrumental settings outlined in Glorie et al. (2017) and Gillespie et al. (2018). Data reduction was carried out using the VisualAge_UcomPbine and X_Trace_Elements_IS data reduction software (DRS) in Iolite (Paton et al., 2011) and IsoplotR was used for U–Pb calculations (Vermeesch, 2018). Regression lines in Tera-Wasserburg plots were all unanchored to allow age calculations without assumptions about the initial (common) Pb isotopic composition (cf. Kirkland et al., 2018a; Glorie et al., 2019). Madagascar apatite (MAD; ID-TIMS age of 473.5 ± 0.7 Ma; Thomson et al., 2012; Chew et al., 2014) was used as the primary reference material for apatite U–Pb age calculations and NIST610 glass was used as the primary standard for trace element concentration determinations. McClure apatite was used as a secondary reference material, yielding a ^{207}Pb-corrected weighted average age of 526 ± 4 Ma. This value is in good agreement to the published ID-TIMS ^{207}Pb/^{235}U age for McClure apatite of 523.51 ± 1.47 Ma (Schoene and Bowring, 2006). Multi-element discrimination (Principal component analysis (PCA) and multiclass Support Vector Machine (SVM) classification) was used to differentiate the source terranes of the samples based on apatite trace-element geochemistry and to compare the apatite trace element data with an extensive published apatite geochemistry database (O'Sullivan et al., 2018, 2020). In more detail, this paper uses the SVM categorization scheme of O'Sullivan et al. (2020), which differentiates alkali-rich igneous rocks (ALK); I-type granitoids and mafic igneous rocks (I + M); low- and medium-grade metamorphic and metasomatic rocks (LM); partial-melts/leucosomes/high-grade metamorphic rocks (HM); S-type and high aluminium saturation index 'felsic' I-type granitoids (S); and ultramafic rocks including carbonatites, lherzolites and pyroxenites

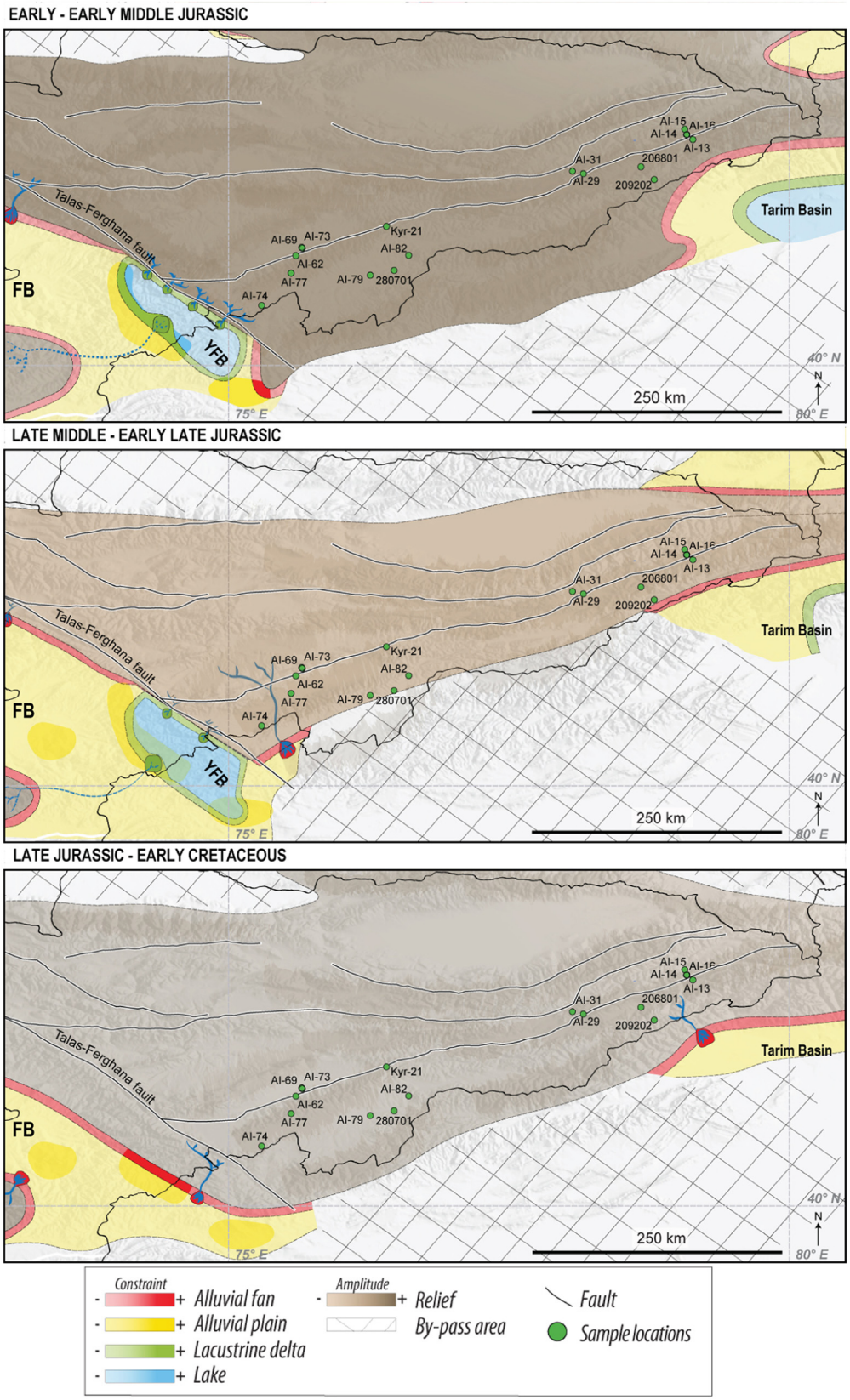

Fig. 2. Digital elevation models for the Kyrgyz South Tian Shan, superimposed by palaeotopographic reconstructions for the Jurassic–early Cretaceous with indication of basement highs (erosion prone area) in grey-brown overlay, inferred Jurassic alluvial fans in red and palaeo-rivers in dark blue (modified from Morin et al., 2018). Sample locations are indicated by green symbols and black font. The figure illustrates that the STS and MTS were largely exposed in basement highs during the Jurassic–early Cretaceous and that the sampled plutons and metamorphic complexes were main suppliers of detritus to the Ferghana, Yarkand-Ferghana (=YFB) and Tarim Basins during that time period.

(UM). Plotting the samples from this work on the PCA biplot clearly differentiates the apatite source terranes and the SVM plot predicts the source lithology based on the published database. Comparing the SVM classifications to the reference sample lithologies for this work not only provides a proof of concept for the discrimination tool, but also enables detection of secondary processes that may have modified the igneous apatites (e.g. Glorie et al., 2019). The resulting classification diagram, in combination with the U–Pb dates, provides a toolbox for future provenance studies in the hydrocarbon-bearing sedimentary basins that surround the Kyrgyz Tian Shan.

4. Results

Sample details and analytical results are documented in Table 1. Apatite U–Pb dates are presented on Tera-Wasserburg concordia diagrams in Fig. 3 and primitive mantle-normalized (McDonough and Sun, 1995) REE concentrations in apatite are displayed on spider plots (using GCD kit; Janousek et al., 2006) in Fig. 4. The full data tables can be found in the Supplementary Materials for this paper. In the sections below, the ranges of mean elemental concentrations between samples within each tectonic unit are specified. Intra-sample concentration variabilities are presented in Figs. 4 and 5 and Supplementary File 2.

4.1. Sary-Dzhaz Range

Five samples from the Sary-Dzhaz Range were analysed, including three samples from the Middle Tian Shan (MTS) and two from the Terektinsky granitic complex along the South Tian Shan suture. Regression lines in the Tera-Wasserburg plots are considered valid when MSWD values are <2 for and this threshold was met for each sample. Apatite U–Pb lower intercept dates are typically <2% RSD at the 2σ level. The apatite U–Pb dates (307 ± 5 Ma and 293 ± 4 Ma; Fig. 3 and Table 1) for the two Terektinsky samples (AI-13 and AI-14) are within uncertainty of the zircon U–Pb dates (302 ± 6 Ma and 294 ± 5 Ma) that were previously obtained for the same samples (Glorie et al., 2011). Similarly, the MTS samples (AI-15, AI-29, AI-31) record apatite U–Pb dates (815 ± 9 Ma, 835 ± 21 Ma, 827 ± 16 Ma; Fig. 3 and Table 1) that correspond well with previously obtained zircon U–Pb age data (831 ± 6 Ma, 842 ± 16 Ma, 806 ± 20 Ma). The two samples (AI-29 and AI-31) with larger age uncertainties (2%–3% for both the apatite and zircon dates) also yield apatite and zircon U–Pb ages within their mutual uncertainties. The more precisely dated sample (AI-15) records a slightly younger apatite U–Pb date (815 ± 9 Ma) compared to its zircon date (831 ± 6 Ma).

Besides the age differences, the two terranes in the Sary-Dzhaz Range exhibit significant differences in apatite trace element compositions. The MTS samples (AI-15, AI-29, AI-31) have low total Rare Earth Element (REE) abundances [(~1–2) × 10^3 ppm], relatively high and consistent Sr concentrations (~580–650 ppm) and low Y concentrations (~220–330 ppm) (Table 1). The primitive mantle-normalized REE plots reveal low negative to flat LREE trends and flat HREE trends and lack Eu anomalies (Fig. 4). In contrast, the Terektinsky samples have higher total REEs [(~6–6.5) × 10^3 ppm], low Sr (~170–190 ppm) and high Y (~980–1150 ppm) concentrations, in addition to large Eu anomalies and strongly negative REE trends (Fig. 4). The PCA biplot confirms the clear distinction between the MTS and Terektinsky samples and the SVM classification plot generally suggests an I-type origin for all Sary-Dzhaz samples, with some geochemical signs for low-temperature metamorphism/metasomatism recorded in the MTS samples only as they extend into the field of low- and medium-grade metamorphic and metasomatic rocks (Fig. 5).

4.2. Kokshaal Range

Seven Kokshaal Range samples were analysed from (leuco)-granite and granodiorite intrusions in the South Tian Shan. The Tera-Wasserburg plots for the Kokshaal samples reveal more data clustering in the upper half of the plots, suggesting greater contributions of initial versus radiogenic Pb than for the Sary-Dzhaz samples, and resulting in slightly larger age uncertainties on the resulting U–Pb lower intercept dates. The regression lines are, however, statistically robust (MSWD values < 1.8 for each sample). The apatite U–Pb dates span a relatively narrow interval of ~298–277 Ma and are all within uncertainties of the published zircon U–Pb dates (~299–279 Ma; Fig. 3 and Table 1) for each sample (Konopelko et al., 2007; Glorie et al., 2011).

The Kokshaal apatite samples furthermore record consistent geochemical signatures with relatively high REE abundances [(~7–11) × 10^3 ppm], low Sr concentrations and high Y concentrations (Table 1). In more detail, samples AI-79 and 280701 from the Kok-Kiya intrusion record consistently slightly higher Sr (~130–135 ppm) and lower Y (~1400–1800 ppm) concentrations compared to the other sampled Kokshaal intrusions (<110 ppm for Sr, > 2300 ppm for Y). The primitive mantle-normalized REE graphs confirm these two groups of trends (Kok-kiya versus other Kokshaal intrusions) with relatively strong negative REE trends for the Kok-kiya samples compared to more flat to low negative REE trends for the other Kokshaal samples (Fig. 4). The Kokshaal apatites can geochemically be distinguished from the other study areas by their significant strong Eu anomalies (Fig. 4). The Djangart sample will not be discussed for its geochemistry due to poor data quality (only 2 grains returned useful geochemical data). On the PCA biplot, the Kok-kiya samples are distinct compared to the other Kokshaal samples, confirming that they can be discriminated in future detrital studies. The SVM classification plot suggests that the Kok-kiya apatites were derived from alkali-rich rocks and an S-type origin for all other Kokshaal samples, without any observed signs of alteration or metamorphism in the apatite chemistries (Fig. 5).

4.3. Atbashi Range

Five samples from the Atbashi Range were analysed from three distinctive tectonic locations: the Tashrabat dioritic intrusion, the Kembel granite/granodiorite and the Atbashi metamorphic complex. The Tera-Wasserburg plots for the Tashrabat and Kembel intrusions reveal a good spread in Pb isotopic compositions, allowing robust regressions and precise apatite U–Pb dates of 289 ± 6 Ma and (416–418) ± 8 Ma, respectively (MSWD values < 2), which are in excellent agreement with published zircon U–Pb dates (Glorie et al., 2011). The apatites in the gneissic Atbashi complex samples yielded very low U concentrations (<2 ppm), resulting in insufficient radiogenic Pb to calculate robust apatite U–Pb dates (Fig. 3, Table 1). The poorly constrained apatite U–Pb dates for the Atbashi Complex are consistent but have large associated uncertainties (454 ± 60 Ma and 450 ± 68 Ma). Although these ages are not reliable, they are significantly younger than a published zircon U–Pb date (788 ± 26 Ma; Glorie et al., 2011), suggesting that the apatites record cooling ages and/or resetting by metamorphism.

The apatite geochemistry for the Atbashi Range samples distinguishes three sample groups that correspond with the three different age groups. The Tashrabat apatites have total REE concentrations of ~6.3 × 10^3 ppm, which are similar to the Terektinsky apatites, but higher Sr (~711 ppm) and lower Y (~718 ppm) concentrations. The Kembel apatites record lower REE abundances [(~4.4–4.9) × 10^3 ppm], similar Y concentrations (~655–700 ppm) but lower Sr (~270–315 ppm) concentrations compared to the Tashrabat samples. The Atbashi Complex samples are distinguished by their very low total REE abundances (<800 ppm) and very high Sr concentrations (~1900–2300 ppm) (Table 1). In primitive mantle-normalized REE graphs, the Kembel and Tashrabat samples reveal similar trends with flat to slightly negative LREE trends and small Eu anomalies. The Tashrabat samples record a more negative HREE trend compared to the Kembel samples. The Atbashi complex samples reveal flat REE trends and lack significant Eu anomalies (Fig. 4). On the PCA biplot, the three different sample groups (Tashrabat, Kembel, Atbashi Complex) can easily be distinguished. The Kembel and Tashrabat samples plot in different locations within the SVM classification field of I-type

Table 1
Sample details, including published zircon U–Pb dates with their 2σ uncertainties for the analysed rock samples (Konopelko et al., 2007; Glorie et al., 2011), the new apatite U–Pb dates with their 95% confidence band uncertainties (95c unc) and a number of common geochemical differentiators for apatite and the resulting SVM category (or categories in case of overlap) for each apatite sample. The full datasets can be found in the Supplementary Files to this paper. The symbols used in the LREE and HREE columns describe the trends in the REE plots (Fig. 4) with + = positive trend, 0 = flat trend, – = slight negative trend, - - = strong negative trend. Eu. refers to the extent of the Eu anomaly in the REE plots (Fig. 4). The ∑REE, Sr, Y and U columns list the mean concentrations of these elements for each sample (with ∑REE = total REE concentration). The SVM column lists the abbreviation for the field(s) in which each element plot (see caption for Fig. 5 for explanation). MTS = Middle Tian Shan, STS=South Tian Shan.

Sample	Latitude (°N)	Longitude (°E)	Terrane	Intrusion/ complex	Lithology	ZU-Pb age	2σ	AU-Pb age	95c unc	LREE	HREE	Eu.	∑REE (10^3 ppm)	Sr (ppm)	Y (ppm)	U (ppm)	Th (ppm)	Th/U	SVM
Sary-Dzhaz Range																			
AI-29	41.7147	78.1636	MTS	Unnamed	Mylonite	806	20	835	21	–	0	none	1.2 ± 0.1	582 ± 5	329 ± 26	7.4 ± 0.7	15.2 ± 1.3	0.64 ± 0.12	I + M/LM
AI-31	41.7367	78.0664	MTS	Unnamed	Felsic Tuff	842	16	827	16	–	0	none	2.0 ± 0.2	649 ± 15	268 ± 20	9.1 ± 2.4	18.4 ± 1.7	0.57 ± 0.11	I + M/LM
AI-15	42.1111	79.0686	MTS	Unnamed	Granite	831	6	815	9	- -	0	none	1.4 ± 0.1	597 ± 4	219 ± 23	10.7 ± 1.9	11.1 ± 1.1	0.98 ± 0.11	I + M/LM
AI-13	42.0643	79.0872	STS - MTS suture	Terektinsky	Granite	302	6	307	5	–	- -	medium	6.0 ± 0.3	190 ± 6	983 ± 54	7.9 ± 1.3	21.0 ± 4.7	0.53 ± 0.12	I + M
AI-14	42.0624	79.0841	STS - MTS suture	Terektinsky	Granite	294	5	293	4	–	- -	medium	6.5 ± 0.3	170 ± 5	1140 ± 45	11.8 ± 1.9	15.8 ± 1.8	0.78 ± 0.09	I + M
Kokshaal Range																			
AI-16	42.0198	79.1404	STS	Tashkoro	Granodiorite	299	4	289	8	–	–	large	10.4 ± 0.9	56 ± 2	2593 ± 255	11.2 ± 1.9	64.5 ± 12.8	0.24 ± 0.01	S
206801	41.7756	78.6772	STS	Uch-Koshkon	Leucogranite	279	8	289	21	–	–	large	8.8 ± 2.2	103 ± 4	2508 ± 248	11.4 ± 6.5	40.5 ± 24.3	0.31 ± 0.01	S
209202	41.6614	78.7958	STS	Djangart	Granite	297	4	298	65	- -	- -	large	NA[a]	NA[a]	NA[a]	NA[a]	NA[a]	NA[a]	S
AI-82	40.9857	76.6052	STS	Mudryum	Granite	286	4	285	15	–	–	large	9.2 ± 0.3	57 ± 8	2315 ± 105	5.7 ± 0.6	21.7 ± 3.1	0.30 ± 0.01	S
AI-74	40.5383	75.2937	STS	Torugart	Granite	288	3	287	9	0	–	large	7.0 ± 0.4	83 ± 3	2372 ± 160	9.9 ± 1.1	30.3 ± 3.9	0.39 ± 0.02	S
AI-79	40.8088	76.2628	STS	Kok-Kiya	Granite	283	4	277	21	- -	- -	large	9.8 ± 0.3	132 ± 2	1461 ± 56	3.9 ± 0.5	12.7 ± 1.8	0.36 ± 0.03	ALK
280701	40.8911	76.5458	STS	Kok-kiya	Leucogranite	279	3	283	28	- -	- -	large	10.7 ± 0.5	134 ± 14	1757 ± 84	4.3 ± 0.5	14.5 ± 1.7	0.31 ± 0.02	ALK
Atbashi Range																			
AI-77	40.8273	75.5565	STS	Tashrabat	Diorite	286	4	289	6	0	- -	small	6.3 ± 0.2	711 ± 4	718 ± 24	18.8 ± 1.6	38.1 ± 2.3	0.49 ± 0.03	I + M
AI-69	41.0497	75.6559	STS - MTS suture	Kembel	Granite	417	5	418	7	–	–	small	4.9 ± 0.2	270 ± 4	655 ± 30	18.5 ± 2.3	36.7 ± 3.1	0.54 ± 0.06	I + M
AI-73	41.0572	75.6515	STS - MTS suture	Kembel	Granodiorite	410	4	416	7	0	–	small	4.4 ± 0.3	315 ± 6	700 ± 41	21 ± 1.8	60.1 ± 5.7	0.42 ± 0.04	I + M
AI-62	40.9833	75.5995	STS - MTS suture	Atbashi	Gneiss	788	26	454	60	0	0	none	0.6 ± 0.1	1914 ± 86	337 ± 16	1.6 ± 0.4	5.0 ± 1.5	1.30 ± 0.36	LM
Kyr-21	41.2439	76.4072	STS - MTS suture	Atbashi	Gneiss	NA[a]	–	450	69	+	0	very small	0.7 ± 0.1	2300 ± 97	494 ± 39	0.9 ± 0.4	4.2 ± 1.7	1.25 ± 0.49	LM

[a] Insufficient data to produce a meaningful average value.

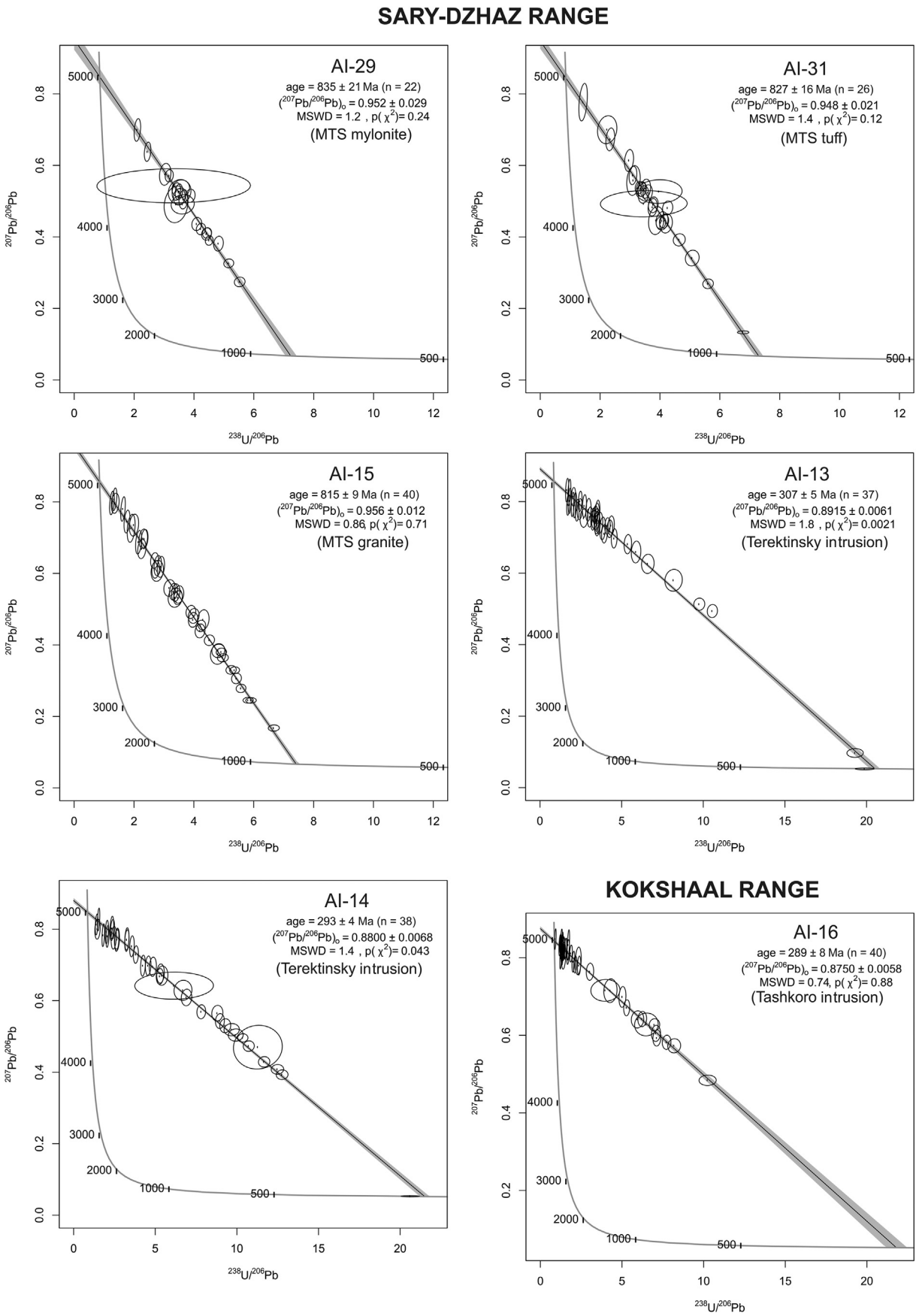

Fig. 3. Tera-Wasserburg concordia diagrams for the apatite samples in this study, calculated in IsoplotR (Vermeesch, 2018). The apatite U–Pb ages were calculated as lower intercept ages from unanchored regression lines for each sample. The reported uncertainties for each date are 95% confidence band uncertainties. MSWD = mean square weighted deviation, $p(\chi^2)$ = chi-square probability (both are measures of goodness of fit in a single population). n = number of analyses.

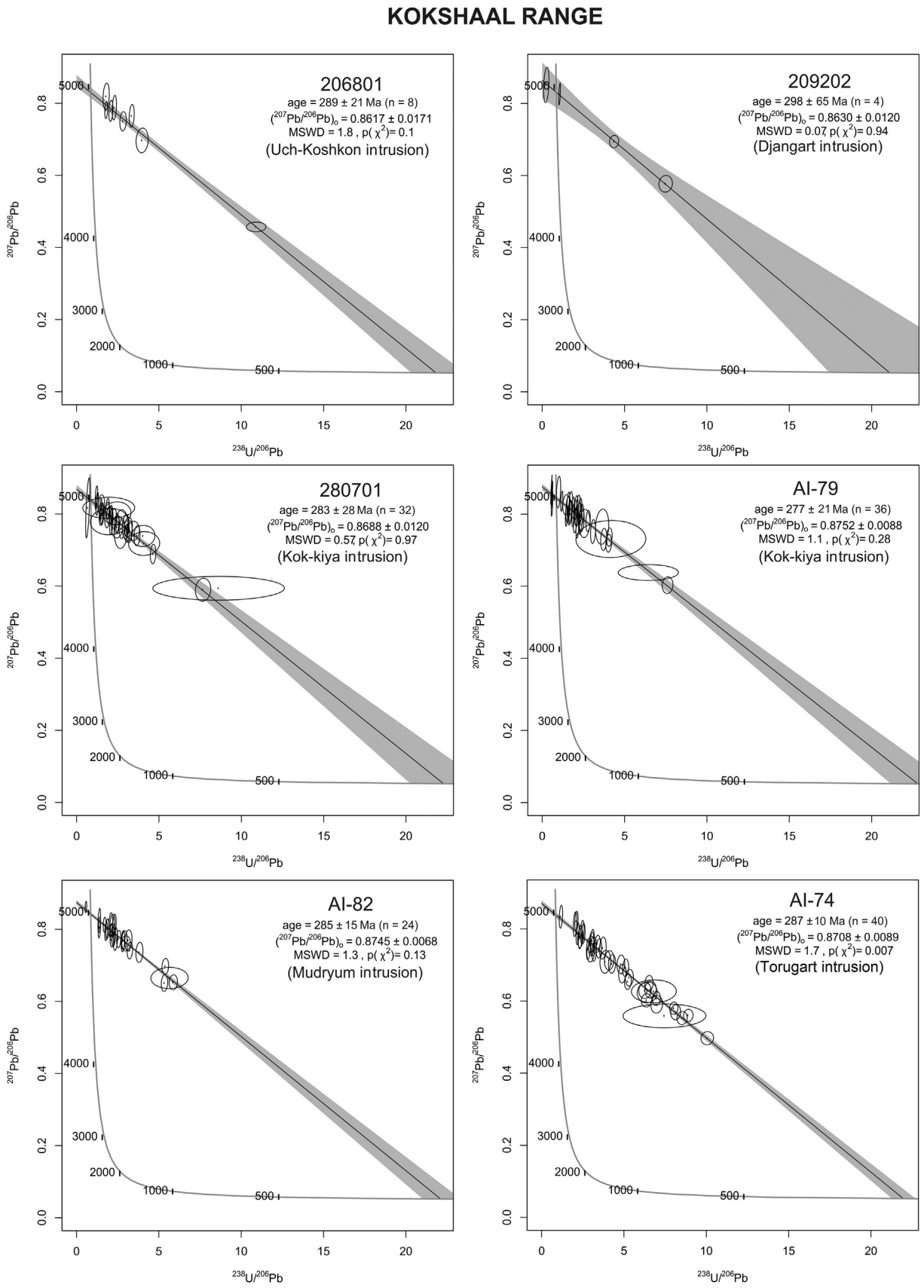

Fig. 3. (*continued*).

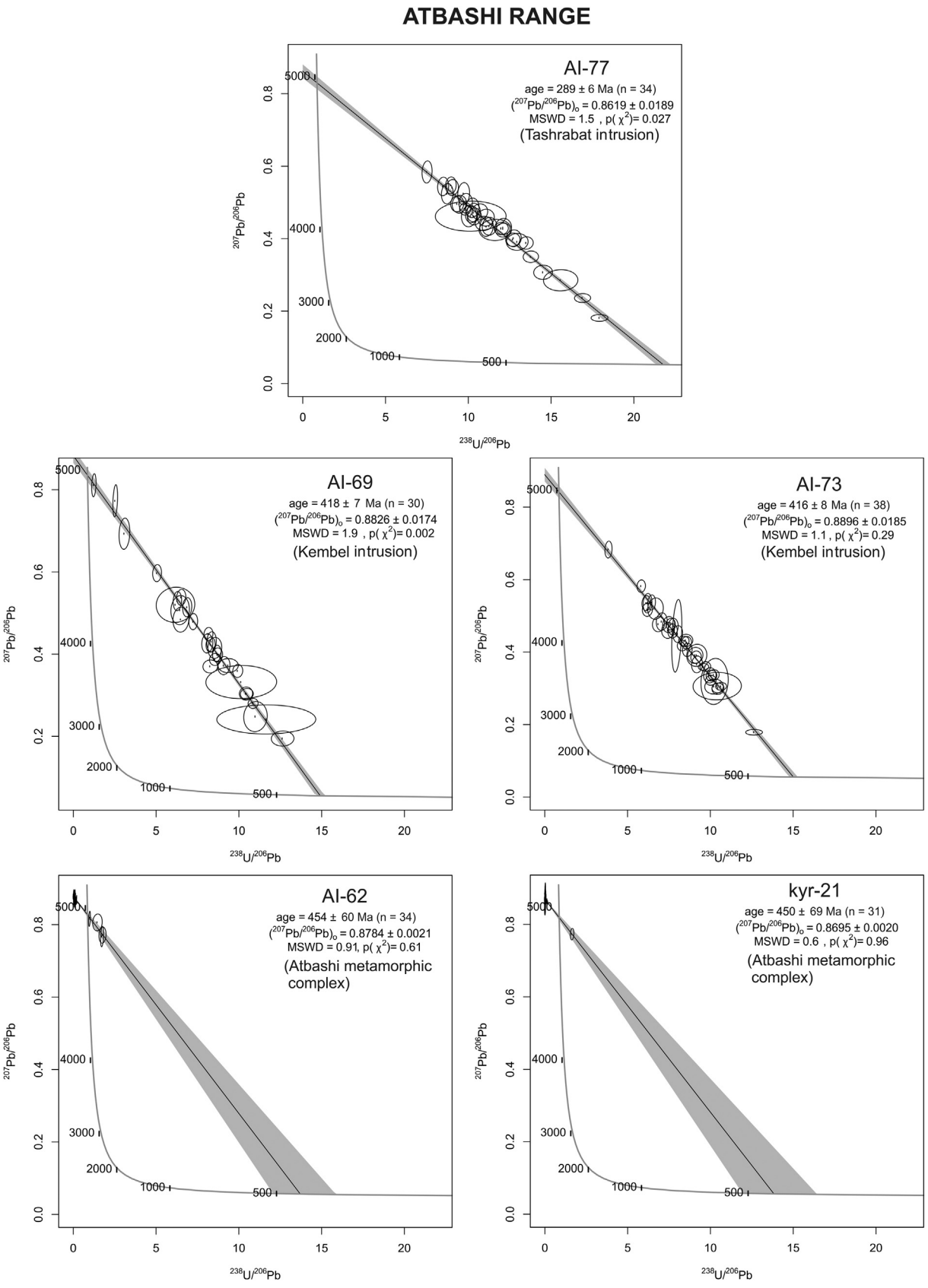

Fig. 3. (*continued*).

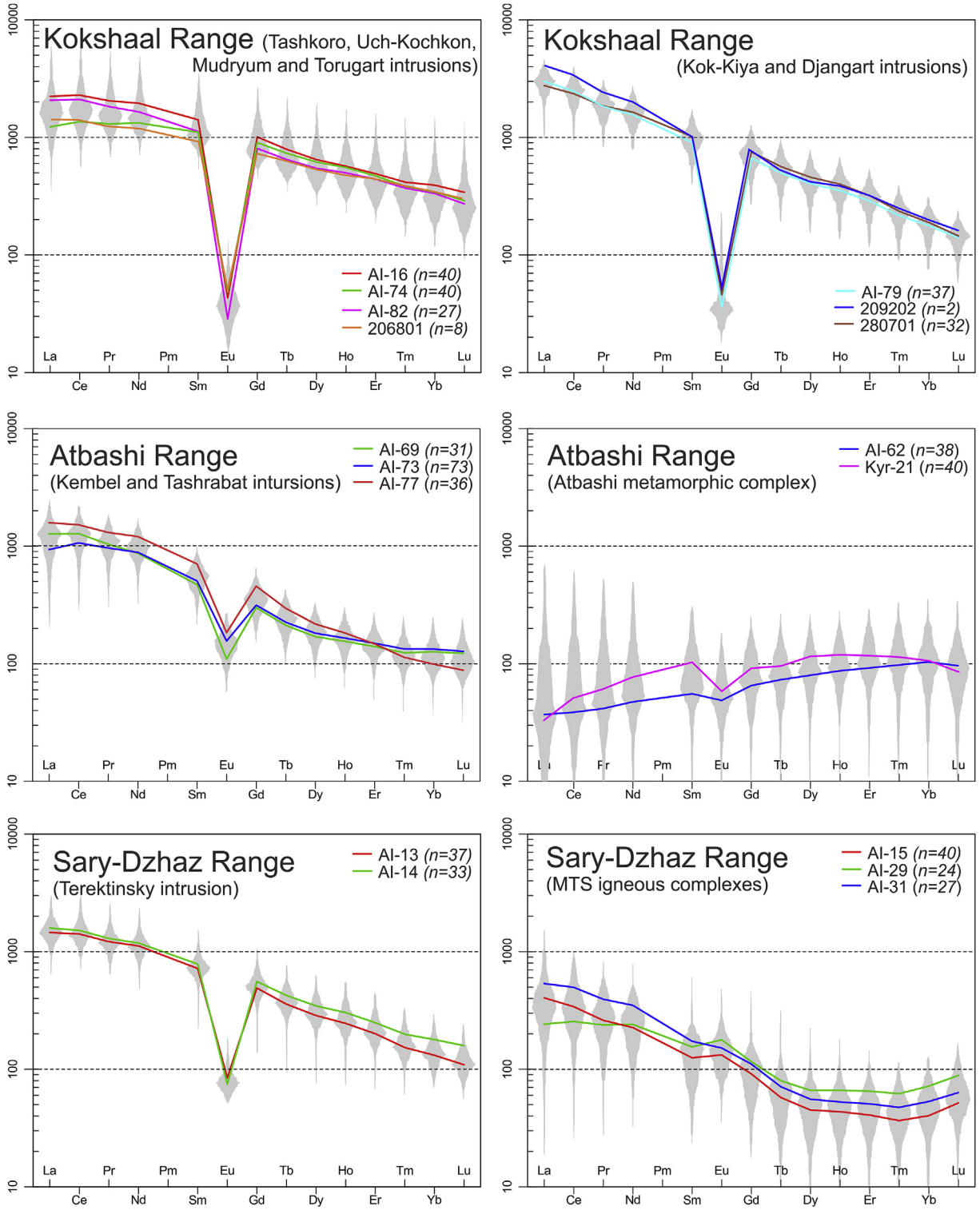

Fig. 4. Primitive mantle-normalized (McDonough and Sun, 1995) Rare Earth Element (REE) trace element spider diagrams, plotted using GCDkit 5.0 (Janousek et al., 2006) for the apatite samples. Sample averages are shown by line graphs and the intra-sample REE data variability is displayed as grey boxplots (n = number of analyses). Whole-rock (WR) data for most of the sampled intrusions can be found in Konopelko et al. (2007 and references therein).

granitoids and mafic igneous rocks, while the Atbashi Complex samples predominantly plot in the low- and medium-grade metamorphic and metasomatic fields with some grains plotting in a similar position on the I-type field as recorded by the MTS samples in the Sary-Dzhaz Range (Fig. 5).

5. Interpretation and discussion

5.1. Apatite geochronology and geochemistry

Table 1 illustrates that the apatite U–Pb dates for most samples are

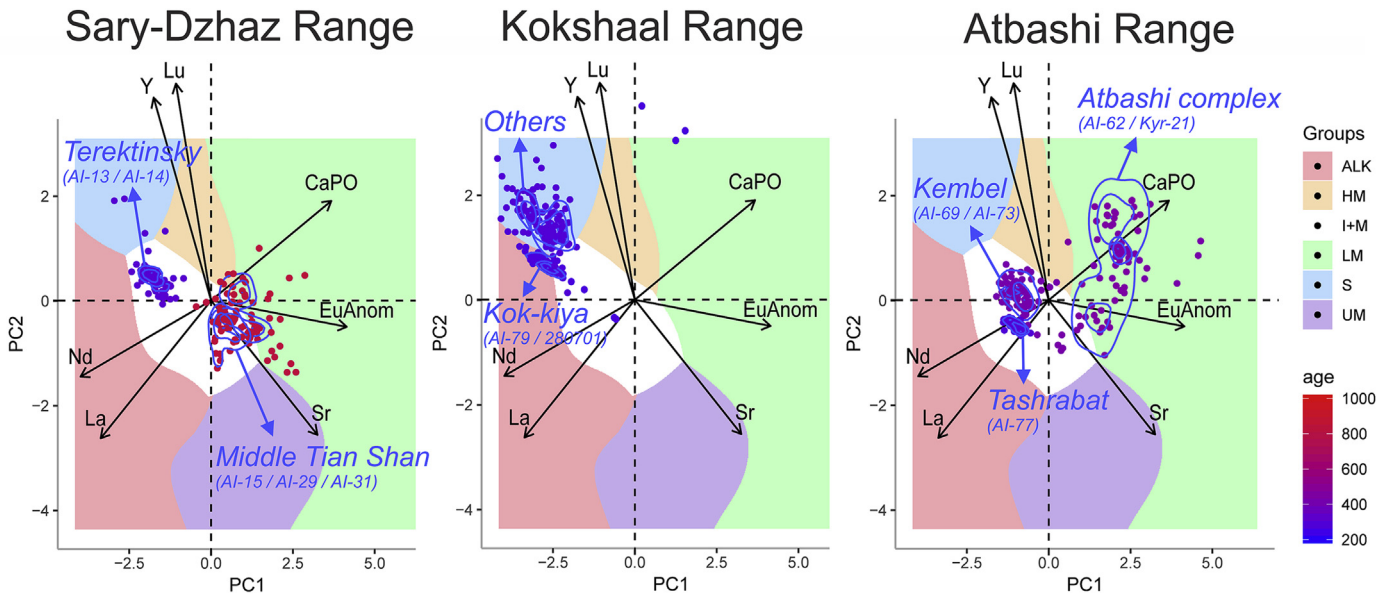

Fig. 5. Principal component analysis (PCA) biplots that differentiate the apatites from this study based on their multi-element trace-element geochemistry, following the PCA scheme in Henrichs et al. (2019) and O'Sullivan et al. (2020), overlain on a support vector machine (SVM) categorization scheme (O'Sullivan et al., 2020) based on the apatite geochemical database from (O'Sullivan et al., 2018). The colour of the symbols corresponds to the apatite U–Pb age for each sample. The figure is used in this paper to test the accuracy of the SVM categorization for the bedrock apatites in the Kyrgyz Tian Shan and to geochemically fingerprint the different plutons and complexes for future provenance studies. The abbreviations for the categorized fields are: ALK = alkali-rich igneous rocks; I + M = mafic I-type granitoids and mafic igneous rocks; LM = low- and medium-grade metamorphic and metasomatic; HM = partial-melts/leucosomes/high-grade metamorphic; S = S-type granitoids and high aluminium saturation index (ASI) 'felsic' I-types; UM = ultramafic rocks including carbonatites, lherzolites and pyroxenites (O'Sullivan et al., 2020).

within uncertainty to the corresponding zircon U–Pb dates. The three exceptions are sample AI-15 from the Sary-Dzhaz Range (minor age difference: 831 ± 6 Ma vs 815 ± 9 Ma) and AI-62 and Kyr-21 from the Atbashi complex (larger age difference: >240 million years). Geochemically, these three samples can be distinguished from all the others by their higher Th/U ratios (~1 for AI-15 and >1 for AI-62 and Kyr-21) and lower ∑REE concentrations (<1500 ppm) (Table 1). Both the depletion in ∑REE and the higher Th/U ratios are indicative of metamorphic apatite (Henrichs et al., 2019), suggesting that the samples record a degree of metamorphic overprinting or fluid alteration and/or regrowth that was undetected by petrology. Hence, the U–Pb dates for these samples may record a metamorphic cooling age or a mixing age between the timing of crystallization and metamorphism (partial Pb diffusion) (Henrichs et al., 2018; Kirkland et al., 2018; O'Sullivan et al., 2018; Glorie et al., 2019). Sample AI-15 from the Sary-Dzhaz Range records a minor age difference between the zircon and apatite U–Pb dates, potentially suggesting limited Pb mobility during metamorphism (discussed further below). The Atbashi complex (samples AI-62 and Kyr-21) underwent high-pressure metamorphism at maximum P–T conditions of 23–25 kbar and 560–570 °C in the metasedimentary melange and 5–6 kbar and 290–340 °C in the accretionary prism (Simonov et al., 2008; Loury et al., 2018). The imprecise (but internally consistent) apatite U–Pb dates (454 ± 60 Ma and 450 ± 69 Ma) for gneissic rocks from the high-pressure metasedimentary melange are significantly older than the timing of peak metamorphism (~328–319 Ma, phengite Ar–Ar dates; Loury et al., 2018) and younger than the zircon U–Pb dates from the same sample (788 ± 26 Ma; Glorie et al., 2011). This may suggest that the apatites experienced extensive Pb mobility during metamorphism and therefore, the resulting apatite U–Pb ages likely represent mixing ages between the timing of protolith emplacement and metamorphism. The Th/U ratios and ∑REE concentrations for both samples plot near amphibolite facies apatites using the relevant biplot from Henrichs et al. (2019), consistent with maximum temperature conditions recorded for the metamorphic complex. The Atbashi complex samples are easily distinguishable by their elevated Sr concentrations and depleted U concentrations as well as by the geochemical discriminators discussed above. Hence, similar to previously published work (e.g. Henrichs et al., 2018, 2019; O'Sullivan et al., 2018), potentially dateable metamorphic apatite within the Kyrgyz Tian Shan can easily be identified using trace-element geochemistry. Noting these few exceptions where metamorphic overprints were detected, the Kyrgyz STS generally preserves primary igneous apatite ages and geochemical signatures, which can be used as a complement to zircon geochronology to accurately trace sedimentary pathways from source (exhumed intrusions in the STS) to sink (e.g. Ferghana, Yarkand-Ferghana and Tarim Basins).

5.2. *Apatite geochemical discrimination in relation to source rock lithology*

The SVM classification (based on the apatite geochemistry PCA biplot) differentiates the late Carboniferous–early Permian granitoid samples into three main categories. The Kok-kiya samples are classified as alkali-rich igneous rocks (ALK field), the Tashrabat and Terektinsky apatites plot within the I + M field (I-type granitoids and mafic igneous rocks) and all other (Kokshaal) apatite samples show S-type and high aluminium saturation index 'felsic' I-type granitoid (S-field) affinities (Fig. 5). The Kokshaal granites are all geochemically characterised as A-type (Konopelko et al., 2007). The apatites in these rocks have relatively low Sr and high Y concentrations (Table 1) and REE patterns with large Eu anomalies (Fig. 4) that mimic those published for whole-rock samples from the same intrusions (Konopelko et al., 2007). The PCA biplot, based on the apatite literature database, predominantly uses the low Sr and high Y (and Lu) concentrations to define the S-field, which are also the characteristics of apatite from A-type granites (Whalen et al., 1987). Only apatites derived from the leucogranitic samples from the Kok-kiya pluton plot entirely in the alkaline field with slightly higher Sr and lower Y concentrations in apatite, compared to the other Kokshaal samples. Hence, A-type granites need to be considered at the interface between the 'S' and 'ALK' fields in the SVM plots (Fig. 5). The Tashrabat and Terektinsky apatite samples plot in distinguishable locations of the 'I + M field' (Fig. 5), for different reasons. The Tashrabat sample is a diorite and thus a more mafic rock, as attested by the higher apatite Sr concentrations (Table 1). Hence, the SVM classifies the apatites correctly as derived

from a mafic igneous rock. The Terektinsky samples have low Sr concentrations and similar REE patterns as the Kokshaal samples, but also lower Y concentrations (Table 1). Whole rock geochemistry confirms an I-type origin (Konopelko et al., 2009), suggesting an accurate classification of these apatite samples.

The apatites from the Early Devonian granitoid rocks from the Kembel intrusion plot in the 'I + M' field on the SVM diagram, suggesting I-type affinity, similar to the Terektinsky intrusion, discussed above (Fig. 5). Thus, if present in detritus, apatite from the Kembel and Terektinsky intrusions would also need to be distinguished by their apatite U–Pb ages (Early Devonian versus late Carboniferous). The MTS apatite samples plot in a different location in the 'I + M' field, with overlap into the 'LM' field and are characterised by low ∑REE and low Y concentrations (Table 1, Fig. 5). The overlap into the 'LM' field is predominantly defined by sample AI-15, which has a slightly younger apatite U–Pb age compared to its zircon age, as discussed above. Hence, the SVM suggests that the age difference between zircons and apatites in sample AI-15 might be related to a minor low-to medium-grade metamorphic or metasomatic overprint. The apatites from the Atbashi metamorphic complex record dispersed compositions on the SVM diagram, which tend to form a mixing line between the location of the MTS apatites in the lower part of the 'I + M' field and the 'LM' field (Fig. 5). Hence, the SVM classification confirms a stronger metamorphic overprint for the apatites from the Atbashi complex, but also suggests partial preservation of an I + M affinity, akin to the MTS granites. Similarity in zircon ages preserved in the Atbashi complex (788 ± 26 Ma) to those in the MTS granitoids (~806–842 Ma) further supports the theory that the precursor of the Atbashi complex has MTS affinity and thus the sampled rocks of the Atbashi complex represent the strongly reworked margin of the MTS terrane. Hence, in addition to a provenance tracer, combined apatite geochronology and geochemistry can be used as a probe to advance knowledge on the protolith composition of strongly metamorphosed terranes.

6. Conclusions and implications for provenance studies

This study has developed a discrimination tool for the basement highs in the Kyrgyz South Tian Shan that supplied detritus to the Ferghana, Yarkand-Ferghana and Tarim Basins in response to Meso–Cenozoic exhumation (Fig. 2; De Pelsmaeker et al., 2018). Combining apatite U–Pb dating with trace-element geochemistry enables successful discrimination of the main intrusive rocks in the Kyrgyz STS (Fig. 5) and allows detection of metamorphic overprints that may complicate detrital spectra. The Kyrgyz STS does not record evidence for significant fluid alteration in the apatite data and instead mostly preserves primary igneous dates and geochemical signatures characteristic of magmatic rocks. Given that apatites are commonly less reworked than zircons, comparing a combined apatite geochronology-geochemistry dataset with similar zircon datasets (which more often represent multi-cycle detritus) may provide enhanced details on sedimentary pathways from source to sink, which are of great importance for basin evolution studies. Hence, this study lays down the foundations for detailed provenance studies by characterizing a major part of the regional basement apatite record. Future studies should continue to develop this framework in different basement terranes that surround the basins to eventually allow multi-mineral provenance studies that include analysis of the contributions of mafic and low to medium temperature metamorphic rock types.

Declaration of competing interest

The authors declare that they have no known competing financial interests or personal relationships that could have appeared to influence the work reported in this paper.

Acknowledgements

This paper was supported by research grant DP200101881 from the Australian Research Council. M. Jolivet and an anonymous reviewer are thanked for their constructive reviews. Sarah Gilbert is thanked for technical assistance with the analytical facilities at Adelaide Microscopy. D. Konopelko acknowledges support from the Ministry of Education and Science of the Russian Federation (Project No. 14. Y26.31.0018) and travel grant from SPbGU (C0LLAB2019_2, Id: 37752801).

Appendix A. Supplementary data

Supplementary data to this article can be found online at https://doi.org/10.1016/j.gsf.2020.06.003.

References

Abdrakhmatov, K.Y., Aldazhanov, S.A., Hager, B.H., Hamburger, M.W., Herring, T.A., Kalabaev, K.B., Makarov, V.I., Molnar, P., Panasyuk, S.V., Prilepin, M.T., Reilinger, R.E., Sadybakasov, I.S., Souter, B.J., Trapeznikov, Y.A., Tsurkov, V.Y., Zubovich, A.V., 1996. Relatively recent construction of the Tien Shan inferred from GPS measurements of present-day crustal deformation rates. Nature 384, 450–453.

Belousova, E.A., Griffin, W.L., O'Reilly, S.Y., Fisher, N.I., 2002. Apatite as an indicator mineral for mineral exploration: trace-element compositions and their relationship to host rock type. J. Geochem. Explor. 76, 45–69.

Belousova, E.A., Griffin, W.L., O'Reilly, S.Y., Fisher, N.I., 2002. Igneous zircon: trace element composition as an indicator of source rock type. Contrib. Mineral. Petrol. 143, 602–622.

Carrapa, B., DeCelles, P.G., Reiners, P.W., Gehrels, G.E., Sudo, M., 2009. Apatite triple dating and white mica $^{40}Ar/^{39}Ar$ thermochronology of syntectonic detritus in the Central Andes: a multiphase tectonothermal history. Geology 37, 407–410.

Cawood, P.A., Hawkesworth, C.J., Dhuime, B., 2012. Detrital zircon record and tectonic setting. Geology 40, 875–878.

Chew, D.M., Petrus, J.A., Kamber, B.S., 2014. U-Pb LA-ICPMS dating using accessory mineral standards with variable common Pb. Chem. Geol. 363, 185–199.

Chew, D.M., Spikings, R.A., 2015. Geochronology and thermochronology using apatite: time and temperature, lower crust to surface. Elements 11, 189–194.

Chew, D.M., Sylvester, P.J., Tubrett, M.N., 2011. U-Pb and Th-Pb dating of apatite by LA-ICPMS. Chem. Geol. 280, 200–216.

Condie, K.C., Belousova, E., Griffin, W.L., Sircombe, K.N., 2009. Granitoid events in space and time: constraints from igneous and detrital zircon age spectra. Gondwana Res. 15, 228–242.

De Grave, J., Glorie, S., Buslov, M.M., Stockli, D.F., McWilliams, M.O., Batalev, V.Y., Van den Haute, P., 2013. Thermo-tectonic history of the Issyk-Kul basement (Kyrgyz Northern Tien Shan, Central Asia). Gondwana Res. 23, 998–1020.

De Grave, J., Glorie, S., Ryabinin, A., Zhimulev, F., Buslov, M.M., Izmer, A., Elburg, M., Vanhaecke, F., Van den Haute, P., 2012. Late Palaeozoic and Meso-Cenozoic tectonic evolution of the southern Kyrgyz Tien Shan: constraints from multi-method thermochronology in the Trans-Alai, Turkestan-Alai segment and the southeastern Ferghana Basin. J. Asian Earth Sci. 44, 149–168.

De Pelsmaeker, E., Jolivet, M., Laborde, A., Poujol, M., Robin, C., Zhimulev, F.I., Nachtergaele, S., Glorie, S., De Clercq, S., Batalev, V.Y., De Grave, J., 2018. Source-to-sink dynamics in the Kyrgyz Tien Shan from the Jurassic to the Paleogene: insights from sedimentological and detrital zircon U-Pb analyses. Gondwana Res. 54, 180–204.

Ding, L.R., 2006. Petroleum geological characteristics and resource potential of Alay Basin in Central Asia. Offshore Oil 26 (4), 29–33 (in Chinese with English abstract).

Gehrels, G., 2011. Detrital Zircon U-Pb Geochronology: Current Methods and New Opportunities. In: Busby, C., Azor, A. (Eds.), Tectonics of Sedimentary Basins: Recent Advances. Blackwell Publishing Ltd, pp. 45–62.

Gillespie, J., Glorie, S., Khudoley, A., Collins, A.S., 2018. Detrital apatite U-Pb and trace element analysis as a provenance tool: insights from the Yenisey Ridge (Siberia). Lithos 314–315, 140–155.

Glorie, S., Agostino, K., Dutch, R., Pawley, M., Hall, J., Danisik, M., Evans, N.J., Collins, A.S., 2017. Thermal history and differential exhumation across the Eastern Musgrave Province, South Australia: insights from low-temperature thermochronology. Tectonophysics 703-704, 23–41.

Glorie, S., Alexandrov, I., Nixon, A., Jepson, G., Gillespie, J., Jahn, B.-M., 2017. Thermal and exhumation history of Sakhalin Island (Russia) constrained by apatite U-Pb and fission track thermochronology. J. Asian Earth Sci. 143, 326–342.

Glorie, S., De Grave, J., 2016. Exhuming the Meso-Cenozoic Kyrgyz Tianshan and Siberian Altai-Sayan: a review based on low-temperature thermochronology. Geosci. Front. 7, 155–170.

Glorie, S., De Grave, J., Buslov, M.M., Elburg, M.A., Stockli, D.F., Gerdes, A., Van den Haute, P., 2010. Multi-method chronometric constraints on the evolution of the Northern Kyrgyz Tien Shan granitoids (Central Asian Orogenic Belt): from emplacement to exhumation. J. Asian Earth Sci. 38 (3–4), 131–146.

Glorie, S., De Grave, J., Buslov, M.M., Zhimulev, F.I., Izmer, A., Vandoorne, W., Ryabinin, A., Van den Haute, P., Vanhaecke, F., Elburg, M.A., 2011. Formation and Palaeozoic evolution of the Gorny-Altai-Altai-Mongolia suture zone (South Siberia): zircon U/Pb constraints on the igneous record. Gondwana Res. 20, 465–484.

Glorie, S., De Grave, J., Buslov, M.M., Zhimulev, F.I., Safonova, I.Y., 2014. Detrital zircon provenance of early Palaeozoic sediments at the southwestern margin of the Siberian Craton: insights from U-Pb geochronology. J. Asian Earth Sci. 82, 115–123.

Glorie, S., De Grave, J., Buslov, M.M., Zhimulev, F.I., Stockli, D.F., Batalev, V.Y., Izmer, A., Van den Haute, P., Vanhaecke, F., Elburg, M.A., 2011. Tectonic history of the Kyrgyz South Tien Shan (Atbashi-Inylchek) suture zone: the role of inherited structures during deformation-propagation. Tectonics 30, TC6016. https://doi.org/10.1029/2011TC002949.

Glorie, S., Jepson, G., Konopelko, D., Mirkamalov, R., Meeuws, F., Gilbert, S., Gillespie, J., Collins, A.S., Xiao, W.J., Dewaele, S., De Grave, J., 2019. Thermochronological and geochemical footprints of post-orogenic fluid alteration recorded in apatite : implications for mineralisation in the Uzbek Tian Shan. Gondwana Res. 71, 1–15.

Hegner, E., Klemd, R., Kroner, A., Corsini, M., Alexeiev, D.V., Iaccheri, L.M., Zack, T., Dulski, P., Xia, X., Windley, B.F., 2010. Mineral ages and P-T conditions of late Paleozoic high-pressure eclogite and provenance of Mélange sediments from Atbashi in the south Tianshan orogen of Kyrgyzstan. Am. J. Sci. 310, 916–950.

Henrichs, I.A., Cheve, D.M., O'Sullivan, G.J., Mark, C., McKenna, C., Guyett, P., 2019. Trace element (Mn-Sr-Y-Th-REE) and U-Pb isotope systematics of metapelitic apatite during progressive greenschist- to amphibolite-facies Barrovian metamorphism. Geochem. Geophys. Geosyst. 20, 4103–4129.

Henrichs, I.A., O'Sullivan, G., Chew, D.M., Mark, C., Babechuk, M.G., McKenna, C., Emo, R., 2018. The trace element and U-Pb systematics of metamorphic apatite. Chem. Geol. 483, 218–238.

Janousek, V., Farrow, C.M., Erban, V., 2006. Interpretation of whole-rock geochemical data in igneous geochemistry: introducing Geochemical Data Toolkit (GCDkit). J. Petrol. 47, 1255–1259.

Jennings, E.S., Marschall, H.R., Hawkesworth, C.J., Storey, C.D., 2011. Characterization of magma from inclusions in zircon: apatite and biotite work well, feldspar less so. Geology 39, 863–866.

Jepson, G., Glorie, S., Konopelko, D., Gillespie, J., Danisik, M., Evans, N.J., Mamadjanov, Y., Collins, A.S., 2018. Thermochronological insights into the structural contact between the Tian Shan and Pamirs, Tajikistan. Terra Nova 30, 95–104.

Jia, Y.Y., Fu, B.H., Jolivet, M., Zheng, S., 2015. Cenozoic tectono-geomorphological growth of the SW Chinese Tian Shan: insight from AFT and detrital zircon U-Pb data. J. Asian Earth Sci. 111, 395–413.

Kirkland, C.L., Fougerouse, D., Reddy, S.M., Hollis, J., Saxey, D.W., 2018. Assessing the mechanisms of common Pb incorporation into titanite. Chem. Geol. 483, 558–566.

Kirkland, C.L., Hollis, J., Danisik, M., Petersen, J., Evans, N.J., McDonald, B.J., 2017. Apatite and titanite from the Karrat Group, Greenland; implications for charting the thermal evolution of crust from the U-Pb geochronology of common Pb bearing phases. Precambrian Res. 300, 107–120.

Kirkland, C.L., Yakymchuk, C., Szilas, K., Evans, N., Hollis, J., McDonald, B., Gardiner, N.J., 2018. Apatite: a U-Pb thermochronometer or geochronometer? Lithos 318, 143–157.

Konopelko, D., Biske, G., Seltmann, R., Eklund, O., Belyatsky, B., 2007. Hercynian post-collisional A-type granites of the Kokshaal Range, Southern Tien Shan, Kyrgyzstan. Lithos 97 (1–2), 140–160.

Konopelko, D., Klemd, R., Petrov, S.V., Apayarov, F., Nazaraliev, B., Vokueva, O., Schersten, A., Sergeev, S., 2017. Precambrian gold mineralization at Djamgyr in the Kyrgyz Tien Shan: tectonic and metallogenic implications. Ore Geol. Rev. 86, 537–547.

Konopelko, D., Seltmann, R., Biske, G., Lepekhina, E., Sergeev, S., 2009. Possible source dichotomy of contemporaneous post-collisional barren I-type versus tin-bearing A-type granites, lying on opposite sides of the South Tien Shan suture. Ore Geol. Rev. 35, 206–216.

Konopelko, D., Wilde, S.A., Seltmann, R., Romer, R.L., Biske, Y.S., 2018. Early Permian intrusions of the Alai range: understanding tectonic settings of Hercynian post-collisional magmatism in the South Tien Shan, Kyrgyzstan. Lithos 302, 405–420.

Lease, R.O., Burbank, D.W., Gehrels, G.E., Wang, Z., Yuan, D., 2007. Signatures of mountain building: detrital zircon U/Pb ages from northeastern Tibet. Geology 35, 239–242.

Loury, C., Rolland, Y., Guillot, S., Lanari, P., Ganino, C., Melis, R., Jourdon, A., Petit, C., Beyssac, O., Gallet, S., Monie, P., 2018. Tectonometamorphic evolution of the Atbashi high-P units (Kyrgyz CAOB, Tien Shan): implications for the closure of the Turkestan Ocean and continental subduction-exhumation of the South Kazakh continental margin. J. Metamorph. Geol. 36, 959–985.

Macaulay, E.A., Sobel, E.R., Mikolaichuk, A., Kohn, B., Stuart, F.M., 2014. Cenozoic deformation and exhumation history of the Central Kyrgyz Tien Shan. Tectonics 33, 135–165.

Mark, C., Cogné, N., Chew, D., 2016. Tracking exhumation and drainage divide migration of the western Alps: a test of the apatite U-Pb thermochronometer. Geol. Soc. Am. Bull. 128.

McDonough, W.F., Sun, S.S., 1995. The composition of the Earth. Chem. Geol. 120, 223–253.

Moecher, D.P., Samson, S.D., 2006. Differential zircon fertility of source terranes and natural bias in the detrital zircon record: implications for sedimentary provenance analysis. Earth Planet Sci. Lett. 247, 252–266.

Morin, J., Jolivet, M., Robin, C., Heilbronn, G., Barrier, L., Bourquin, S., Jia, Y.Y., 2018. Jurassic paleogeography of the Tian Shan: an evolution driven by far-field tectonics and climate. Earth Sci. Rev. 187, 286–313.

Morin, J., Jolivet, M., Shaw, D., Bourquin, S., Bataleva, E., 2020. New sedimentological and palynological data from the Yarkand-Fergana Basin (Kyrgyz Tian Shan): insights on its Mesozoic paleogeographic and tectonic evolution. Geosci. Front. (in press). https://doi.org/10.1016/j.gsf.2020.04.010.

Nachtergaele, S., De Pelsmaeker, E., Glorie, S., Zhimulev, F., Jolivet, M., Danisik, M., Buslov, M.M., De Grave, J., 2018. Meso-Cenozoic tectonic evolution of the Talas-Fergana region of the Kyrgyz Tien Shan revealed by low-temperature basement and detrital thermochronology. Geosci. Front. 9, 1495–1514.

O'Sullivan, G., Chew, D., Kenny, G., Henrichs, I., Mulligan, D., 2020. The trace element composition of apatite and its application to detrital provenance studies. Earth Sci. Rev. (in press). https://doi.org/10.1016/j.earscirev.2019.103044.

O'Sullivan, G.J., Chew, D.M., Morton, A.C., Mark, C., Henrichs, I.A., 2018. An integrated apatite geochronology and geochemistry tool for sedimentary provenance analysis. Geochem. Geophys. Geosyst. 19, 1309–1326.

Otto, S.C., 1997. Mesozoic-Cenozoic history of deformation and petroleum systems in sedimentary basins of Central Asia: implications of collisions on the Eurasian margin. Petrol. Geosci. 3, 327–341.

Paton, C., Hellstrom, J., Paul, B., Woodhead, J., Hergt, J., 2011. Iolite: freeware for the visualisation and processing of mass spectrometric data. J. Anal. Atomic Spectrom. 26, 2508–2518.

Schoene, B., Bowring, S.A., 2006. U-Pb systematics of the McClure Mountain syenite: thermochronological constraints on the age of the $^{40}Ar/^{39}Ar$ standard MMhb. Contrib. Mineral. Petrol. 151, 615–630.

Seltmann, R., Konopelko, D., Biske, G., Divaev, F., Sergeev, S., 2011. Hercynian post-collisional magmatism in the context of Paleozoic magmatic evolution of the Tien Shan orogenic belt. J. Asian Earth Sci. 42, 821–838.

Simonov, V.A., Sakiev, K.S., Volkova, N.I., Stupakov, S.I., Travin, A.V., 2008. Conditions of formation of the Atbashi ridge eclogites (south Tien Shan). Russ. Geol. Geophys. 49, 803–815.

Sobel, E.R., 1999. Basin analysis of the Jurassic-Lower Cretaceous southwest Tarim basin, northwest China. Geol. Soc. Am. Bull. 111, 709–724.

Sobel, E.R., Chen, J., Heermance, R.V., 2006. Late Oligocene-early Miocene initiation of shortening in the southwestern Chinese Tian Shan: implications for Neogene shortening rate variations. Earth Planet Sci. Lett. 247, 70–81.

Sobel, E.R., Oskin, M., Burbank, D., Mikolaichuk, A., 2006. Exhumation of basement-cored uplifts: example of the Kyrgyz Range quantified with apatite fission track thermochronology. Tectonics 25, TC2008. https://doi.org/10.1029/2005TC001809.

Thomson, S.N., Gehrels, G.E., Ruiz, J., Buchwaldt, R., 2012. Routine low-damage apatite U-Pb dating using laser ablation-multicollector-ICPMS. Geochem. Geophys. Geosyst. 13 (1), Q0AA21. https://doi.org/10.1029/2011GC003928.

Vermeesch, P., 2018. IsoplotR: a free and open toolbox for geochronology. Geosci. Front. 9 (5), 1479–1493.

Watson, M.P., Hayward, A.B., Parkinson, D.N., Zhang, Z.M., 1987. Plate tectonic history, basin development and petroleum source rock deposition onshore China. Mar. Petrol. Geol. 4, 205–225.

Whalen, J.B., Currie, K.L., Chappell, B.W., 1987. A-type granites - geochemical characteristics, discrimination and petrogenesis. Contrib. Mineral. Petrol. 95, 407–419.

Windley, B.F., Alexeiev, D., Xiao, W.J., Kroner, A., Badarch, G., 2007. Tectonic models for accretion of the Central Asian Orogenic Belt. J. Geol. Soc. 164, 31–47.

Yang, W., Jolivet, M., Dupont-Nivet, G., Guo, Z.J., 2014. Mesozoic - Cenozoic tectonic evolution of southwestern Tian Shan: evidence from detrital zircon U/Pb and apatite fission track ages of the Ulugqat area, Northwest China. Gondwana Res. 26, 986–1008.

Zhu, Y., Liu, L., Lin, C., 2005. Petroleum geology of Fergana Basin in Central Asia. J. Lanzhou Univ. (Natural Sciences) 41 (1), 25–31 (in Chinese with English abstract).

Zhukov, Y.B., Zaharov, L.A., Berezanskii, L.A., Izranleva, P.M., 2008. Geological Map of the Kyrgyz Republic, Scale 1:500.000. Agency of Geol. And Mineral. Resour. of the Kyrgyz Repub., Bishkek, Kyrgystan.